

# Endwall geometric uncertainty and error on the performance of TUDA-GLR-OpenStage transonic axial compressor

## Original article

### Article history:

Submission date: 23 October 2022

Acceptance date: 27 February 2023

Publication date: 31 March 2023

This is the updated version of a paper originally presented at the Global Power and Propulsion Technical Conference, GPPS Chania22, September 11–14, 2022.



### \*Correspondence:

XH: xiao.he2014@imperial.ac.uk

### Peer review:

Single blind

### Copyright:

© 2023 Xia et al. © This is an open access article distributed under the Creative Commons Attribution Non Commercial No Derivatives License (CC BY-NC-ND 4.0). Unrestricted use, distribution, and reproduction of the original work are permitted for noncommercial purposes only, provided it is properly cited and its authors credited. No derivative of this work may be distributed.

### Keywords:

compressor aerodynamics; tip leakage flow; corner separation; validation and verification; cavity flow

### Citation:

Xia K., He X., Zhu M., Klausmann F. S., Teng J., and Vahdati M. (2022). Endwall geometric uncertainty and error on the performance of TUDA-GLR-OpenStage transonic axial compressor. *Journal of the Global Power and Propulsion Society*. 7: 113–126.  
<https://doi.org/10.33737/jgpps/161708>

Kailong Xia<sup>1</sup>, Xiao He<sup>2,\*</sup>, Mingmin Zhu<sup>1</sup>, Fabian Sebastian Klausmann<sup>3</sup>, Jinfang Teng<sup>1</sup>, Mehdi Vahdati<sup>2</sup>

<sup>1</sup>School of Aeronautics and Astronautics, Shanghai Jiao Tong University, Shanghai 200240, China

<sup>2</sup>Department of Mechanical Engineering, Imperial College London, London SW7 2AZ, UK

<sup>3</sup>Institute of Gas Turbines and Aerospace Propulsion, Technische Universität Darmstadt, Darmstadt 64287, Germany

## Abstract

The hub and casing walls of axial compressors are often modeled as smooth continuous surfaces in CFD simulations, but in real geometries, non-smooth pinches, steps and leakage cavities may exist. In the GPPS first Turbomachinery CFD Workshop, a comprehensive validation and verification campaign of RANS flow solvers was conducted, and all the simulation results consistently over-predicted the total pressure ratio at the rotor exit near the casing and the stator exit near the hub. From a recent examination of the test rig geometry, a pinched casing wall over the rotor and a leakage cavity below the stator were found, which were not considered in the workshop. In this paper, the effects of these endwall geometric uncertainties and errors are analyzed via numerical simulation. When considering the rotor casing pinch of the test geometry, the predicted total pressure ratio and choke mass flow of the compressor stage are smaller than that without the pinch, leading to better agreement with the measured data. When considering a stator hub cavity with a leakage flow rate of about 0.2% of the compressor inlet mass flow, the near-hub total pressure ratio distribution matches slightly better with the experimental data, but the effects on the global compressor stage characteristics are not visible. The relevant mechanisms of these changes in performances are analyzed in detail. The updated geometries and grids will be released to the public as a benchmark test case for turbomachinery CFD validation and verification.

## Introduction

Due to the manufacturing tolerance, assembly requirements and hot geometry effects, geometric uncertainty and error of axial compressors arise, especially near the endwall regions. These uncertainties and errors are important reasons for the inconsistency between the CFD predictions and the experimental data (Denton, 2010; Gourdain et al., 2014). Some examples of the endwall geometric error include: (1) the rotor casing pinch, which often has a polyline/curvy shape but can be oversimplified to a straight line; (2) the stator hub cavity, which is often ignored in the CFD model but can have a visible effect on the near-hub flow field. In the following, the effects of casing endwall shape and hub cavity on the compressor performances are briefly reviewed.

Regarding the casing endwall shape, several configurations including casing recess/trench and casing axisymmetric contouring have been studied in previous research. A systematic investigation of recessing the casing over the rotor tips conducted by Wisler and Beacher (1989) indicated that the increase of tip clearances and rotor penetration into the trench will result in loss of efficiency in a four-stage compressor. On the contrary, Thompson et al. (1998) and Beheshti et al. (2004) found that the stepped-tip gaps machined into the rotor casing can improve pressure ratio, efficiency and stall margin in transonic compressors. Sun et al. (2018) studied the influence of various axisymmetric endwall contours on a high-load low-reaction transonic rotor, and both the shock structure and the separation location were found to be sensitive to the endwall meridional configurations. Kröger et al. (2011) investigated the axisymmetric contouring for subsonic compressor rotors with large clearance heights and found that it reduces the tip clearance losses and endwall blockage.

Regarding the hub cavity, extensive studies have been conducted on the loss mechanism of hub leakage flows. For the commonly used open test case NASA Rotor 37, the discrepancy between the measured data and early CFD simulations near 40% span was believed to be caused by neglecting a 0.75 mm gap between the rotor disk and the stationary center body (Moore and Reid, 1980; Denton, 1997; Chima, 2009); more recent CFD simulations confirmed that the axial gap can generate such a deficit even when there is zero net leakage (Shabbir et al., 1997; Castillon et al., 2014; Seshadri et al., 2014). For stators with a hub cavity, detrimental effects of the leakage flow were usually reported: Wellborn and Okiishi (1999) performed a comprehensive investigation of the effect of stator hub leakage flow on the primary passage flow in a four-stage low-speed compressor, and the leakage flow was found to increase blockage, deviation, and thus total pressure loss near the stator hub; Demargne and Longley (2000) experimentally investigated the cavity effect on a linear compressor cascade, and the total pressure loss was found to increase with the leakage mass flow rate. However, cases for which the cavity leakage flow brings beneficial effects do exist: Sohn et al. (2006) found that increasing the tangential velocity of the leakage flow can reduce the secondary flow and therefore the overall loss in a shrouded compressor cascade; Lei et al. (2008) and Zhu et al. (2019) reported that the leakage flow can delay the stall onset in a compressor cascade and in a transonic compressor stage.

After the GPPS first Turbomachinery CFD Workshop, a careful inspection of the TUDa-GLR-OpenStage geometry has been performed, and a rotor casing pinch and a stator hub cavity were found. These geometric uncertainties and errors were not considered in the workshop CFD model, which potentially explains the over-prediction of total pressure ratio in the previous validation attempts (He et al., 2023). The goal of this paper is to elaborate on the effects of these geometric uncertainties and errors on the aerodynamic performances of TUDa-GLR-OpenStage. In the following, details of the test compressor, the updated endwall geometries and the numerical methods will be introduced first, followed by the analysis of the rotor casing pinch effects and the stator hub leakage effects. Concretely, the overall performance and the radial profiles will be compared, and the loss mechanisms will be analyzed.

## Numerical methodology

---

### Baseline compressor

The investigated TUDa-GLR-OpenStage is a single-stage high-speed axial compressor, representing a typical front stage of a high-pressure compressor in a commercial turbofan engine. The compressor stage, as shown in Figure 1, includes a blisk rotor with 16 radially stacked CDA-airfoils, an optimized 3D-shaped stator with 29 blades, and an outlet guide vane (OGV) that straightens the flow. The crucial design parameters of the investigated stage can be found in Klausmann et al. (2022). The rotor was initially designed and tested by MTU in 1994 and has been investigated extensively in a series of research (Hoeger et al., 1999; Bergner et al., 2006; Muller et al., 2011). The rotor blades are highly cambered near the hub and thin near the tip. At the design condition, the rotor running tip gap size is approximately 0.75 mm, and the rotor hub fillet radius is 5 mm. The stator is designed conjointly between GLR and German Aerospace Center (DLR). It was optimized via an automated multi-objective optimization process to suppress the separation size (Bakhtiari et al., 2015). The stator blades have a forward sweep feature near both endwalls and a bow feature towards the pressure surface near the casing. The shapes of the stator fillets at both endwalls are prescribed by a digitized geometry file.

The TUDa-GLR-OpenStage was tested on the transonic compressor rig of GLR, which can measure the steady-state performance, the aerodynamic instabilities, and the blade vibration levels of the compressors. The schematic of the test facility is shown in Figure 1. Before reaching the compressor core, the inlet flow passes through an inlet throttle, a settling chamber and a mass flow measurement section. The pressure and temperature measured in the settling chamber reflect the incoming flow property. At the compressor core inlet section

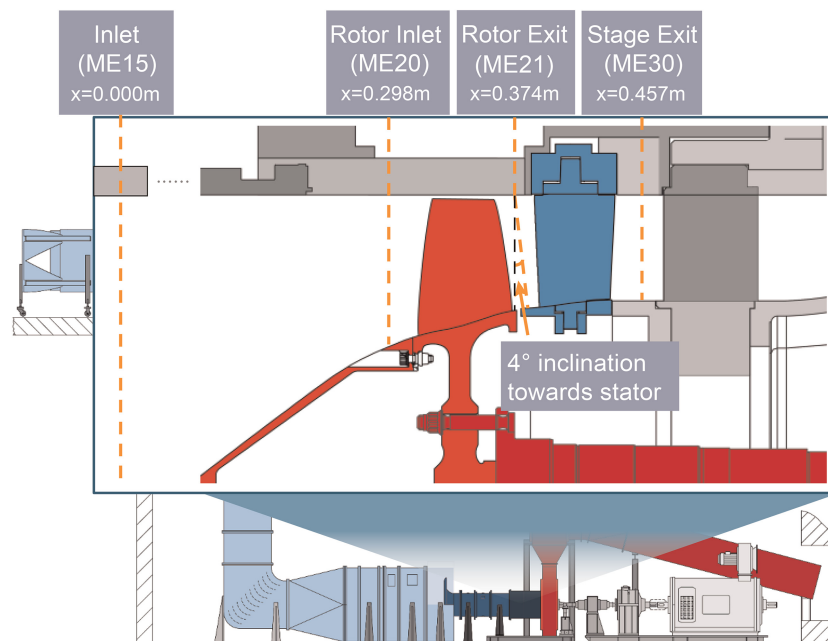


Figure 1. Illustration of TUDA-GLR-OpenStage test rig.

ME15, the total pressure profile of the incoming flow is measured by a boundary layer rake, and the total temperature profile is assumed to be uniform, with its value the same as that measured at the settling chamber (i.e., neglecting the heat transfer effect). The total pressure and total temperature measured at the settling chamber are used to correct the mass flow and the rotational speed to the International Standard Atmosphere (ISA) condition. A DC motor with a gearbox drives the compressor. Shaft input torque and rotor speed is measured using a torque meter. Further details of the experimental setup can be found in [Klausmann et al. \(2022\)](#).

The quantities of interest in the measurement campaign include the rotor exit profile at section ME21, the stator exit profile at section ME30 and the overall performance of the compressor. Among the overall performance quantities, the total pressure ratio  $\pi^*$  and the total temperature ratio  $\tau^*$  are calculated by the area-averaged probe data at sections ME15 and ME30; the isentropic efficiency  $\eta^*$  is calculated using the probe-based  $\pi^*$  and the shaft power. For a fair comparison between the experiment and CFD,  $\pi_{\text{CFD}}^*$  and  $\tau_{\text{CFD}}^*$  are based on the area-averaged quantities, whereas  $\eta_{\text{CFD}}^*$  is based on the area-averaged  $\pi_{\text{CFD}}^*$  and mass-averaged  $\tau_{\text{CFD}}^*$ .

### Endwall configuration

After a careful examination of the manufactured compressor geometry, the CAD geometry model and the CFD geometry model, the differences between the measured and the workshop geometries are summarized as follows:

1. The axial gap between the rotor hub and the stator hub is connected by a smooth curved line in the workshop geometry, whereas from the inspection of the test bench, a polyline is more accurate.
2. The rotor casing endwall is a smooth straight line in the workshop geometry, but a pinch is found in the test bench, as illustrated in [Figure 2](#).
3. A leakage cavity is found beneath the stator in the test bench, which was not included in the workshop geometry. Although the leakage passage should have been effectively sealed in the experiment, the exact seal shape and thus the leakage flow rate remains uncertain due to the hot geometry effect. In this research, a self-designed leakage seal geometry shown in [Figure 2](#) is investigated numerically. This seal geometry is similar to the cold geometry used in the experiment in terms of the minimum seal clearance. Due to intellectual property protection, the measured seal geometry is not presented in this research.

Based on these differences, four cases are investigated in this paper as summarized in [Table 1](#). The performance difference between Case 1 and Case 2, or the difference between a smooth hub and a polyline hub, is not visible in terms of performance characteristics and radial profiles. These results are not shown and discussed for brevity. By comparing Case 2 with Case 3, the effect of the rotor casing pinch can be analyzed, and the relevant results will be presented in Sec. 3. By comparing Case 3 with Case 4, the effect of the stator hub cavity can be investigated, which will be presented later in Sec. 4.

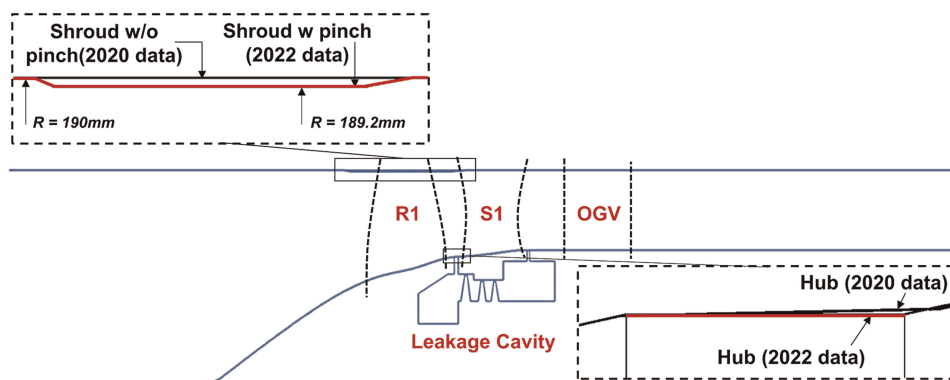


Figure 2. Meridional schematic diagram of endwall contours.

### CFD solver

The commercial three-dimensional Reynolds-Averaged Navier-Stokes flow solver, Ansys CFX (version 2021), is used to perform the steady simulations in this paper. Ansys CFX uses an element-based finite volume method to discretize the RANS equations based on unstructured meshes. It uses an implicit coupled solver that solves all the hydrodynamic equations as a single system. The linearized equations are solved by the Incomplete Lower Upper (ILU) factorization technique, accelerated by an algebraic multigrid method. A pseudo-time-stepping algorithm with an automatic time scale technique is used for steady-state calculations. For the best practice of turbomachinery simulation, the Menter  $k - \omega$  Shear Stress Transport (SST-2003) turbulence model (Menter et al., 2003) and the second-order accurate high-resolution advection scheme (ANSYS, 2021) are recommended.

### Grid topology and boundary conditions

In this work, Numeca AutoGrid5 is used to generate the grids. The main flow region of the rotor, the stator and the OGV are meshed using the O4H-type topology; the rotor tip clearance is meshed using the butterfly topology; the inlet duct, the outlet duct and the leakage path are meshed using the H-type topology. To achieve good resolution in the boundary layer, the area-average  $y^+$  values of the rotor grid and the stator grid are 1.05 and 1.28, respectively. Endwall features including clearances and fillets of the rotor and the stator are considered. The final grids for a periodic passage of the rotor, the stator, the OGV and the leakage path have 3.3, 1.8, 0.8 and 2.1 million grid points, respectively. Such a grid density is the same as that of the fine mesh in the previous work (He et al., 2023), which has met the grid independence requirement (i.e., discretization error of total pressure ratio below 0.7%).

The flow domain and boundary conditions are illustrated in Figure 3. The flow domain contains one blade passage for each blade row, with the periodic boundary condition applied to the side boundaries. The inlet plane is set at the stage inlet section ME15, whose boundary conditions are prescribed by the total pressure and temperature profiles from the experiment at the design speed<sup>1</sup>. An outlet duct of 1.5 times the compressor axial length is

Table 1. Endwall meridional curve configurations.

Case	Shroud Curve	Hub Curve
1	smooth without pinch	smooth without cavity
2	smooth without pinch	polyline without cavity
3	polyline with pinch	polyline without cavity
4	polyline with pinch	polyline with cavity

<sup>1</sup>The inlet profile at 80% speed was not available when the simulations were performed. For consistency, the inlet profile at 100% speed was used.

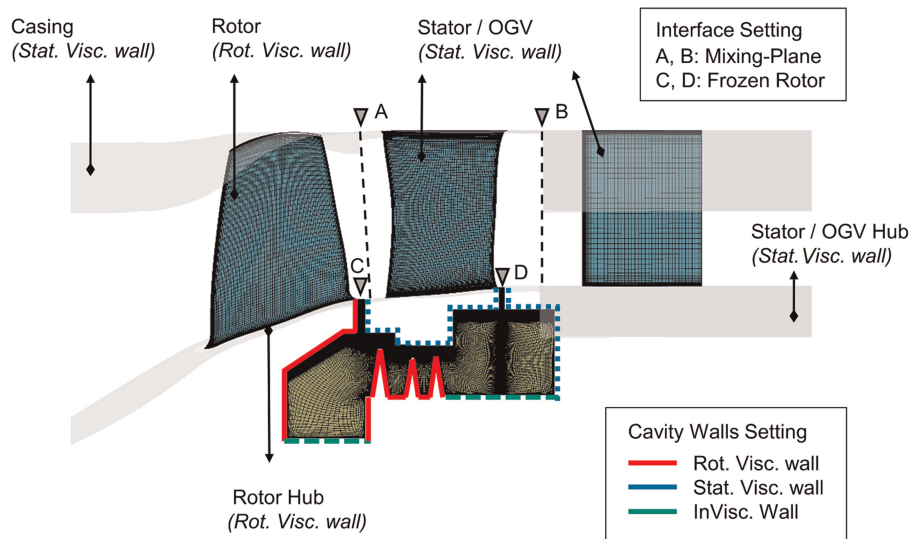


Figure 3. Illustration of grid topology, flow domain and boundary conditions of TUDA-GLR-OpenStage.

attached to the OGV outlet. The radial equilibrium backpressure boundary condition is imposed at the outlet, and the difference in the average backpressure between the adjacent operating points is 100 Pa when approaching the stall limit. At the rotor-to-stator and stator-to-OGV interface, the mixing plane boundary condition is used. In the case of the stator hub cavity, the grids of the primary flow passage are the same as that without the cavity. At the rotor-to-cavity and stator-to-cavity interface, the frozen rotor boundary condition is used.

### Effects of rotor casing pinch

#### Overall performance

The stage performance characteristics with and without the rotor casing pinch are presented in Figure 4. In these plots, the solid curves with open symbols represent simulation results; the solid squares denote the experimental data; the error bars represent the measurement uncertainty<sup>2</sup>. Results show that the trapezoid-shaped pinch moves the  $\pi^*$  and  $\eta^*$  characteristics curves towards the low mass flow direction, which is due to a reduction in the rotor throat area. Such a translation effect becomes more evident when increasing the operating speed. Consequently, the case with the rotor casing pinch shows a better agreement with the measured data. Specifically at the design speed, the casing pinch reduces the total pressure ratio by 0.03 and 0.01 at the PE and the NS points; the casing pinch also reduces the efficiency by 0.2% at the PE point and increases it by 0.9% at the NS point.

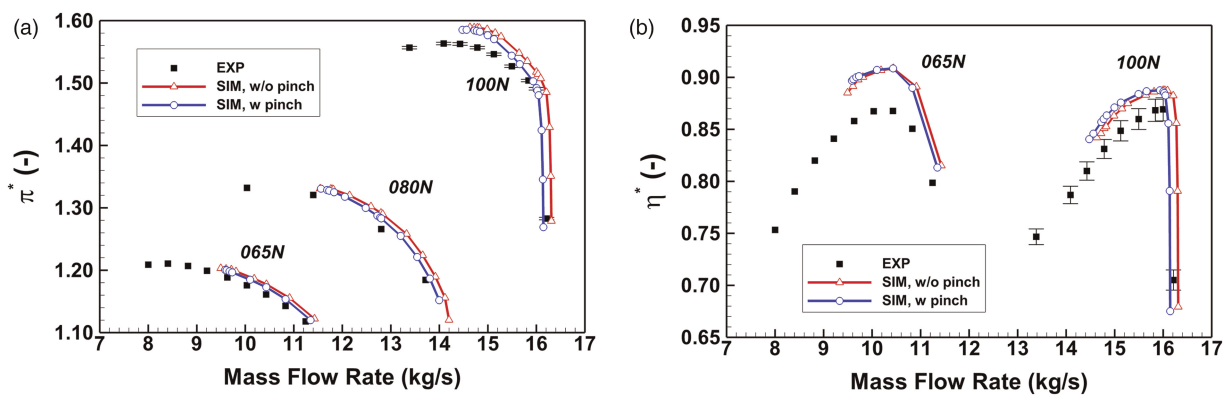


Figure 4. Effect of rotor casing pinch on predicting the TUDA-GLR-OpenStage performance characteristics. (a) total pressure ratio (b) isentropic efficiency.

<sup>2</sup>Currently only the measurement uncertainty at 100% speed is available.

### Radial profiles

To examine the effect of rotor casing pinch in detail, the circumferentially area-averaged radial profiles downstream of the rotor and the stator are presented in Figure 5. In these plots, the hollow squares and circles denote the experimental results, and the curves represent the simulation results.

For the rotor exit profiles shown in Figure 5a, the rotor casing pinch reduces total pressure ratio  $\pi^*$  and absolute flow angle  $\alpha^*$  especially at the upper 50% spans and at the PE condition. Note that the major effect of the pinch is a reduced throat area of the rotor. When comparing at the same mass flow, the case with the pinch will have a lower incidence at the upper spans and thus a reduced work input and  $\pi^*$ . Since the slope of the  $m - \pi^*$  characteristic is steeper at the PE condition than the NS condition, as shown previously in Figure 4a, the performance quantities at the PE condition are more susceptible to the incidence change introduced by the pinch. Comparing both simulation results with the measured data, the pinch case matches better with the measured  $\pi^*$  and  $\alpha^*$ ; in particular,  $\alpha^*$  is predicted with good accuracy, but minor deficiency of  $\pi^*$  persists near 90% span. Such deficiency can be caused by the turbulence model deficiency or the asymmetric untwisting effect of the running geometry (Lu et al., 2019), which was observed during concurrent PIV measurements and needs further investigation.

For the stage exit profiles shown in Figure 5b, the pinch-induced reduction of  $\pi^*$  and work input generally propagates from the rotor to the stator, leading to better agreement with the measured data. The pinch case shows good accuracy in predicting  $\tau^*$  at both PE and NS conditions, but it still over-predicts  $\pi^*$  at the lower 20% spans of the PE condition and the lower 60% spans of the NS condition. Such an over-prediction is not observed in the rotor exit profile. Hence, it is likely caused by the stator hub geometric uncertainty and error (e.g., hub cavity).

To reveal the pinch effect at part speeds, the radial profiles at 65% speed are exhibited in Figure 5c and d. In general, the observations at 65% speed are similar to that at 100% speed: the pinch slightly reduces  $\pi^*$ ,  $\alpha^*$  and  $\tau^*$  at the upper 50% spans at both the PE and NS conditions, leading to better agreement with the measured

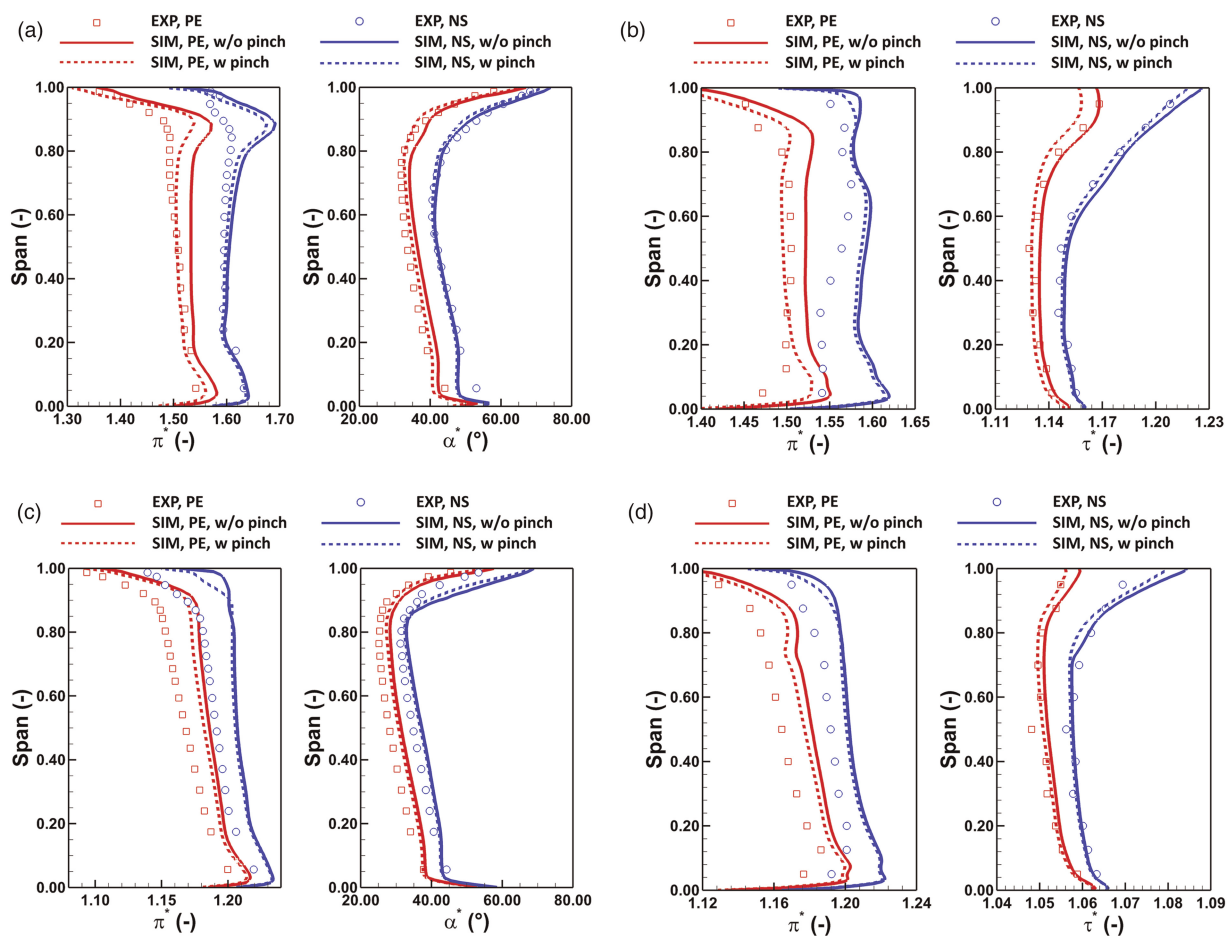


Figure 5. Effect of rotor casing pinch on predicting the circumferentially mass-averaged radial profiles. (a) 100% speed, rotor exit (ME21). (b) 100% speed, stage exit (ME30). (c) 65% speed, rotor exit (ME21). (d) 65% speed, stage exit (ME30).

data. The differences are mainly twofold. Firstly, the pinch-induced reduction of  $\pi^*$ ,  $\alpha^*$  and  $\tau^*$  at the PE condition of 65% speed is less significant than that of 100% speed. This is because the slope of the  $m - \pi^*$  characteristic is steeper (i.e., more sensitive to the incidence change induced by the pinch) at the PE condition at 100% speed than that of 65% speed, as shown previously in Figure 4a. Secondly, the rotor exit  $\pi^*$  and stage exit  $\pi^*$  are over-predicted at all spans at 65% speed, whereas only the near-casing rotor exit  $\pi^*$  and the near-hub stage exit are over-predicted at 100% speed. This can potentially be explained by the error in the inlet boundary condition and the rotor running tip clearance size, whose values are measured at the 100% speed. For future research, the values measured at the 65% speed need to be tested.

### Loss mechanism analysis

The rotor casing pinch is expected to change the rotor near-casing flow field and therefore the local entropy production. In this section, the mechanism by which the pinch changes the compressor efficiency is analyzed in detail. The analysis is based on the streamwise efficiency deviation  $\Delta\eta(m)$  and the spanwise efficiency deviation  $\Delta\eta(n)$  (Appendix A), which measure the difference of the dimensionless entropy between the smooth casing case and the pinched casing case. In other words,  $\Delta\eta(m)$  and  $\Delta\eta(n)$  represent the efficiency gain from the pinched casing at the given streamwise coordinate  $m$  or spanwise coordinate  $n$ .

The streamwise efficiency deviation is plotted against the normalized axial location in Figure 6a. In this plot, solid curves and dashed curves represent the PE condition and the NS condition, respectively. Each of these curves is composed of 58 points in the axial direction, with the  $\Delta\eta$  value of each point calculated from Equation 3 in Appendix A. The horizontal axis represents the axial location normalized by the axial distance between the stage inlet and the exit (bottom axis) or by the rotor axial tip chord (top axis). In general, the change of  $\Delta\eta$  for all the cases occurs mainly in the rotor passage; the net change of  $\Delta\eta$  at the stage exit is about 0.1% for the PE conditions and 0.7% for the NS conditions at both 65% and 100% speed, which is consistent with the data presented in Figure 4. For the PE condition at 100% speed,  $\Delta\eta$  increases initially between  $-1.0$  and  $0.5 C_t$  and then drops between  $0.5$  and  $1.5 C_t$ , which indicates two competing flow mechanisms change the rotor efficiency simultaneously. For the NS condition at 100% speed,  $\Delta\eta$  not only increases between  $-1.0$  and  $0.5 C_t$  but between  $2.2$  and  $3.3 C_t$ , implying the rotor casing pinch reduces loss in the stator. For the other conditions at 65% speed,  $\Delta\eta$  increases before  $0.5 C_t$  and then stays at a similar level in the downstream locations, indicating the rotor casing pinch has a neutral effect on the downstream stator.

To help pinpoint the change of efficiency further, the spanwise efficiency deviation at the stage exit is illustrated in Figure 6b, where the  $\Delta\eta$  value is calculated from Equation 4 in Appendix A. For the PE condition at 100% speed, the pinch increases efficiency between 75% and 95% span but reduces it between 10% and 75% span. For the other conditions, the pinch generally increases the efficiency in the upper 50% span.

Based on the observations in Figure 6, the following regions of flow have evident effects on the compressor efficiency and hence need investigation:

1. The region between  $-1.0$  and  $0.5 C_t$  and between 75% and 95% span at the PE condition of 100% speed, where the pinch increases the local efficiency.

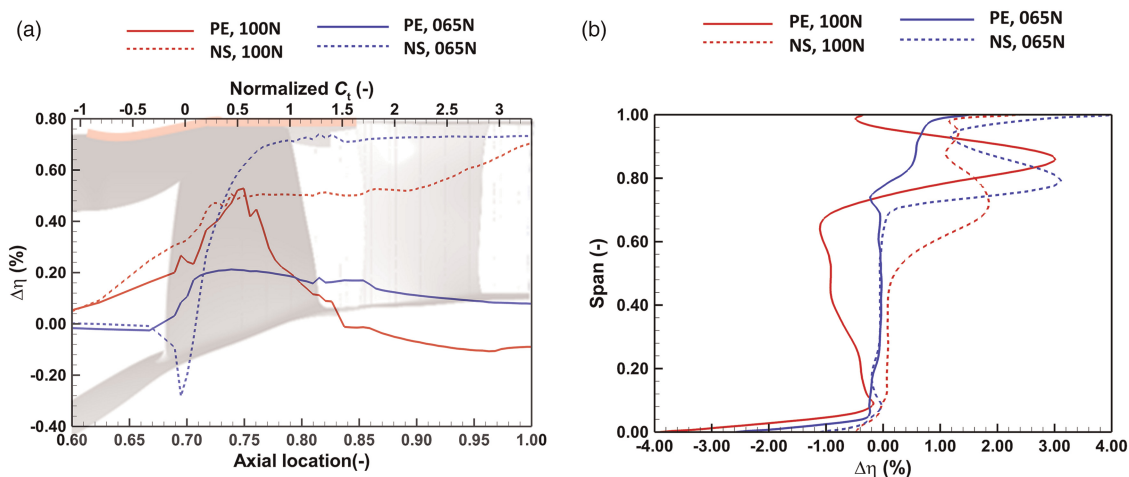


Figure 6. Distribution of efficiency deviation between cases with and without the rotor casing pinch. (a) Streamwise distribution. (b) Spanwise distribution.

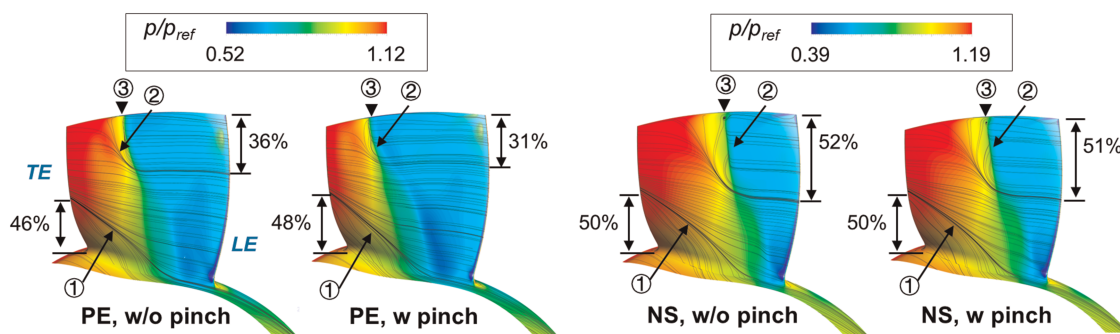


Figure 7. Meridional view of static pressure contour and surface streamlines on the hub surface and the suction surface of the rotor; ①: corner separation; ②: shock-induced separation; ③: shock front.

2. The region between 0.5 and 1.5  $C_t$  and between 10% and 75% span at the PE condition of 100% speed, where the pinch reduces the local efficiency.
3. The region between  $-1.0$  and  $0.5 C_t$  and between 50% and 100% span at the NS condition of both speeds, where the pinch increases the local efficiency.

Regarding the PE and NS conditions at 100% speed, the static pressure contours and the limiting streamlines on the rotor suction surface and the rotor hub surface are presented in Figure 7. For all the cases presented, a hub corner separation and a shock-induced tip separation are observed. At the PE condition, the pinch pushes the shock front to a further downstream location, reduces the spanwise regions affected by the tip separation (from 36% to 31% span) and thus reduces the loss near the casing; on the other hand, the pinch also enlarges the hub corner separation size (from 46% to 48% span), which increases the loss near the hub. These competing flow mechanisms are responsible for the bump shape of  $\Delta\eta$  shown in Figure 6a. At the NS condition, the pinch also reduces the spanwise location affected by the tip separation (from 52% to 51% span), but it has an almost neutral effect on the hub corner separation. Therefore, the net contribution to efficiency is higher in the NS condition than in the PE condition.

Regarding the NS condition of 65% speed, the relative Mach number contours and the relative streamlines are compared in Figure 8. In both cases, a tip leakage vortex is formed due to the shear between the tip leakage flow and the main flow. The difference is that the blockage cell featured by the low Mach number is smaller in the case with the pinch. Therefore, the pinch reduces the mixing loss associated with the tip blockage cell.

### Effects of stator hub cavity

#### Overall performance

The stage performance characteristics with and without the stator hub cavity are presented in Figure 9, where the simulation results are represented by the solid curves with open symbols and the measured data are represented by the solid squares. From the first glance of Figure 9, there are no visible changes in the global performance characteristics with or without the cavity. Further examinations of the characteristic values of the compressor

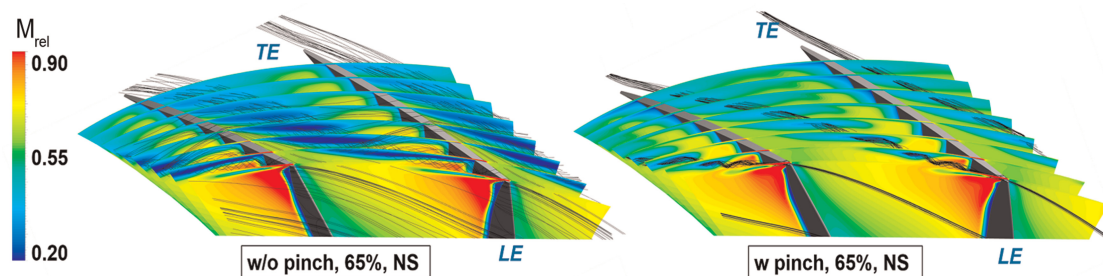


Figure 8. Relative Mach number contour and relative streamlines in the rotor passage with and without the rotor casing pinch.

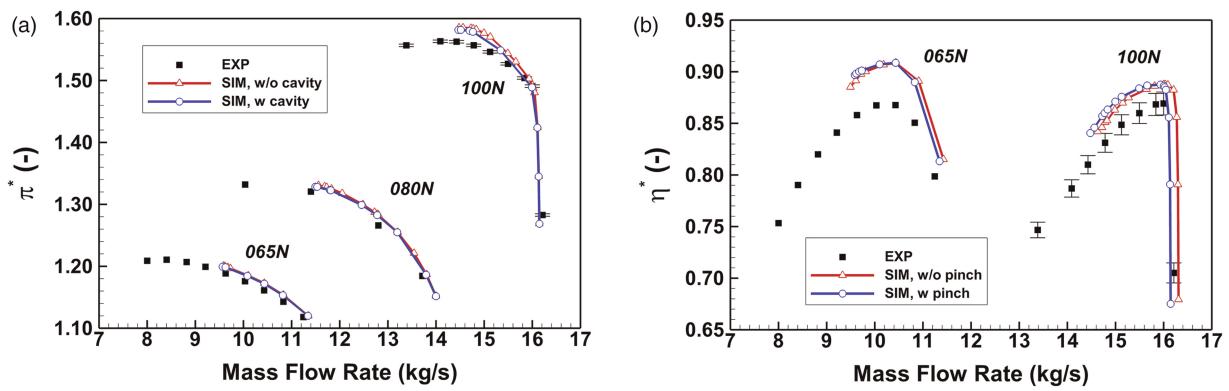


Figure 9. Effect of stator hub leakage flow on predicting the TUDA-GLR-OpenStage performance characteristics. (a) total pressure ratio. (b) isentropic efficiency.

performance quantities show that the cavity does not change  $\pi^*$  and  $m_c$ , but it reduces  $\eta^*$  by 0.5% and 0.4% at 100% and 65% speeds, respectively. Such an effect slightly improves the agreement with the experiment.

The stator hub cavity effect is proportional to the cavity leakage flow rate. In Figure 10, the simulated leakage-to-inlet mass flow ratio is plotted against the inlet mass flow rate. It shows that the investigated cavity seal only allows between 0.15% to 0.25% of leakage-to-inlet mass flow ratio at the PE and NS conditions. According to the previous research (Wellborn and Okiishi, 1999), a leakage mass flow ratio of 0.25% only leads to an efficiency penalty between 0.2% and 0.6% in a multistage compressor, which is consistent with the observations in this work. Although the stator hub cavity investigated in this work does not have an evident effect on the global performance, its effects on the local flow fields still need further check.

### Radial profiles

To examine the effect of the stator hub cavity in detail, the circumferentially area-averaged radial profiles downstream of the stator are presented in Figure 11, where the hollow scatters denote the experimental results and the curves represent the simulation results. Results show that the cavity does not affect the distribution of  $\tau^*$ , which is expected because  $\tau^*$  is mainly dependent on the rotor work input. The effect of the cavity is mainly on the near-hub  $\pi^*$  prediction: at the PE condition of 100% speed, the NS condition of 100% speed and the NS condition of 65% speed, the largest reduction of  $\pi^*$  by the cavity is 2.1%, 2.2% and 1.3%, respectively. According to the previous research on an earlier version of the TUDA-GLR-OpenStage compressor (Zhu et al., 2019), a leakage mass flow ratio of 0.3% can lead to a 1% to 2% reduction in total pressure ratio below the 20% span, which is consistent with the current research. Although the inclusion of the stator hub cavity slightly improves the agreement with the measured data, deficiency persists especially at the NS condition at 100% speed. This is likely caused by the under-estimation of the seal throat area in the current simulation. Further parametric study of the seal throat area is needed to confirm this hypothesis.

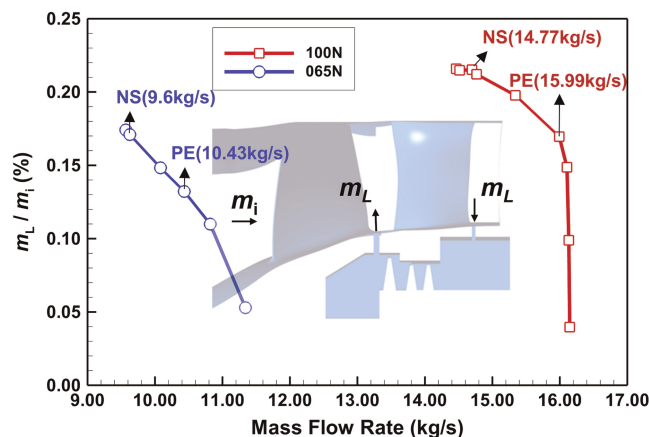


Figure 10. Proportion curve of leakage flow to mainstream under different rotational speed conditions.

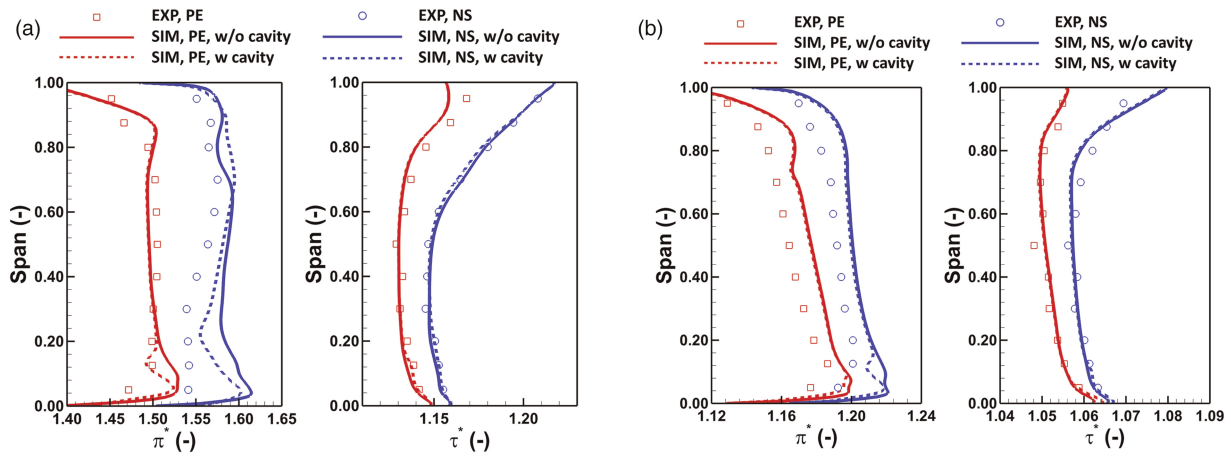


Figure 11. Effect of stator hub cavity on predicting the circumferentially mass-averaged radial profiles. (a) 100% speed, stage exit (ME30). (b) 65% speed, stage exit (ME30).

### Loss mechanism analysis

The stator hub cavity is expected to change the stator near-hub flow fields and therefore, the local entropy production. In this section, the mechanism by which the cavity changes the compressor efficiency is analyzed via the streamwise efficiency deviation  $\Delta\eta(m)$  and the spanwise efficiency deviation  $\Delta\eta(n)$  (Appendix A). In this context,  $\Delta\eta(m)$  and  $\Delta\eta(n)$  represent the efficiency change due to the stator hub cavity leakage at the given streamwise coordinate  $m$  or spanwise coordinate  $n$ .

For the streamwise development of efficiency deviation shown in Figure 12a,  $\Delta\eta$  for all cases stays at almost the same value in the rotor passage, indicating the stator hub cavity has limited effects on the upstream rotor: at the front end of the stator hub cavity,  $\Delta\eta$  suddenly drops due to the mixing with the injected high-entropy leakage flow: at the rear end of the cavity,  $\Delta\eta$  immediately increases due to the bleeding of the high-entropy leakage flow. For the spanwise distribution of efficiency deviation shown in Figure 12b, the efficiency penalty due to the stator hub cavity is at the lower 30% spans. The observations above suggest that the flow field of the stator near the hub has a noticeable effect on the compressor efficiency. Since the results of 65% speed are similar but less evident than that of 100% speed, only the PE and NS conditions at 100% speed will be presented for brevity.

The static pressure contours and the limiting streamlines on the stator suction surface and the stator hub surface are presented in Figure 13. For the PE condition of 100% speed, a hub corner separation and a near-tip

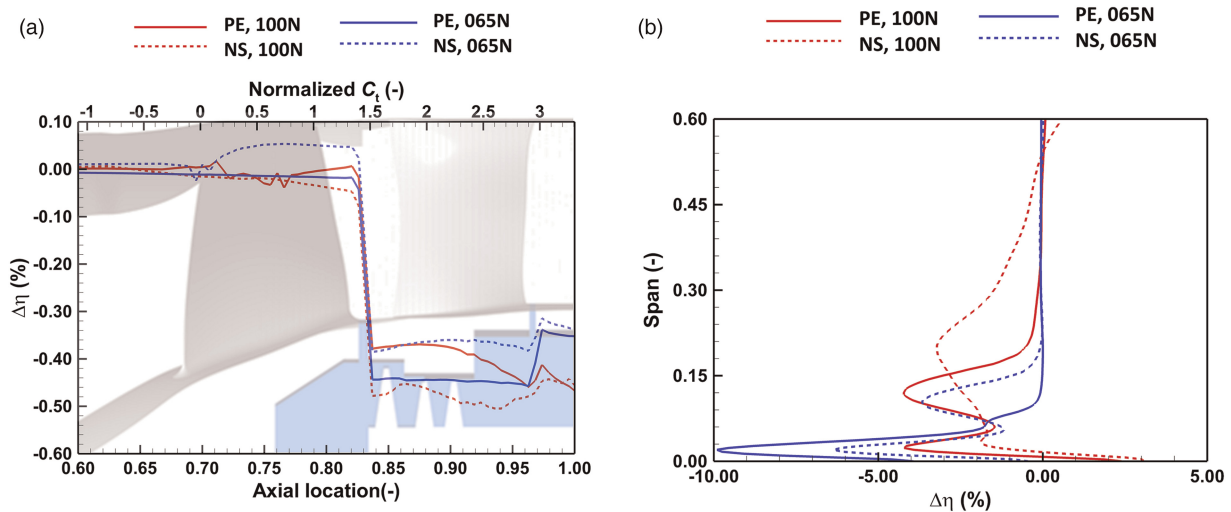


Figure 12. Distribution of efficiency deviation between cases with and without the stator hub cavity. (a) Streamwise distribution. (b) Spanwise distribution.

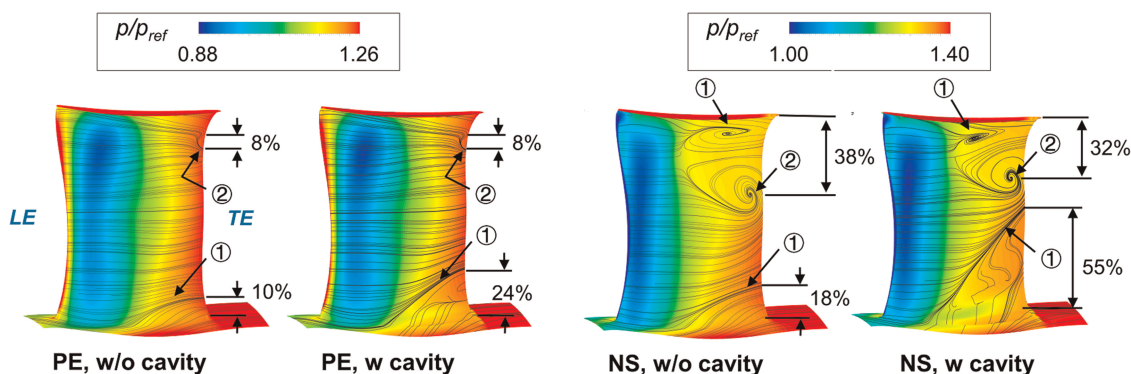


Figure 13. Meridional view of static pressure contour and surface streamlines on the hub surface and the suction surface of the stator; ①: corner separation; ②: trailing edge separation.

trailing edge separation are observed. When considering the stator hub cavity, the hub corner separation size is enlarged (from 10% to 24% span), but the near-tip trailing edge separation is not affected. For the NS condition of 100% speed, a hub corner separation, a mid-span trailing edge separation and a tip corner separation are observed. The cavity again increases the size of hub corner separation (from 18% to 55% span), but the mid-span separation and near-tip separation are barely affected (slightly reduced from 38% to 32% span). The increment of corner separation size at the NS condition is larger than that at the PE condition, which is due to a higher leakage mass flow rate shown in Figure 10. Therefore, it can be concluded that the stator hub cavity leakage enhances the hub corner separation and hence reduces the compressor efficiency and total pressure ratio. Such an effect will become more prominent if the leakage flow ratio increases (i.e., larger seal throat area).

## Conclusions

In this paper, the effects of endwall geometric uncertainty and error on the performance of the TUDA-GLR-OpenStage transonic axial compressor have been investigated via numerical simulations. The flow mechanisms behind the changes in compressor performances have been analyzed. The main conclusions are drawn as follows:

1. The pinched rotor casing translates the rotor characteristics curve towards the low mass flow direction, leading to a reduced choke mass flow and total pressure ratio at all speeds and an increased isentropic efficiency at partial speeds. In terms of the radial profiles, the pinch reduces the total pressure ratio and the work input but increases the isentropic efficiency in the upper 50% span. The underlying flow mechanism leading to the efficiency increase is the reduction of tip blockage size, which is due to the tip unloading effect induced by the pinch.
2. The stator hub cavity leakage reduces slightly the total pressure ratio and the isentropic efficiency, but it has a neutral effect on the choke mass flow and the work input. In terms of the radial profiles, the reduction of total pressure ratio and isentropic efficiency remains in the lower 30% spans. The underlying flow mechanism leading to the efficiency drop is the enlargement of stator hub corner separation. When the leakage-to-inlet mass flow ratio increases, such phenomena become more prominent and hence the larger reduction of the total pressure ratio and the isentropic efficiency.
3. After considering the rotor casing pinch and the stator hub cavity in the CFD model, a better agreement between the experiment and CFD is achieved. Specifically, the former improves the accuracy of the global compressor performance characteristics and the local near-tip profiles; the latter improves the accuracy of the local near-hub profiles. However, the visible difference between the experimental data and the CFD still persists. To reduce this difference, further work is required on both the experiment side and the CFD side. Regarding the experiment, a second measurement campaign is in progress, which aims to reproduce the first measurement data with a higher spatial resolution near the endwalls. Regarding the CFD, the effects of the grid quality, the realistic boundary conditions, and scale-resolving simulation methods are under evaluation. The updated measurement data and CFD model will be provided in the GPPS second turbomachinery CFD workshop.

## Nomenclature

---

### Latins and Greeks

$c_p$	specific heat capacity (J/(kg·K))
$m$	mass flow rate (kg/s)
$M$	Mach number (–)
$p_t$	total pressure (Pa)
$T_t$	total temperature (K)
$\alpha^*$	absolute flow angle (from axial) (deg)
$\Delta\eta$	efficiency deviation (–)
$\eta^*$	isentropic efficiency (–)
$\pi^*$	total pressure ratio (–)
$\tau^*$	total temperature ratio (–)

### Subscripts

$e$	exit
$h$	hub
$i$	inlet
$l$	leakage flow
$m$	mid-span
$rel$	relative frame
$t$	tip

### Abbreviations

EXP	experiment
NS	near stall
PE	peak efficiency
RANS	Reynolds-averaged Navier-Stokes
SIM	simulation
SST	shear stress transport

## Appendix A: Definition of efficiency deviation

---

From the work of Denton (1993), the loss of efficiency of a compressor  $\xi$  can be written as Equation 1:

$$\xi = \frac{T_{t,e}(S_e - S_i)}{c_p(T_{t,e} - T_{t,i})} \approx 1 - \eta^* \quad (1)$$

where  $T_{t,i}$  and  $T_{t,e}$  are the total temperature at the inlet and the exit;  $S_i$  and  $S_e$  are the entropy at the inlet and the exit;  $c_p$  is the specific heat capacity. The approximation arises due to the assumption that  $T_{t,e} \approx T_{t,e,isen}$ , where  $T_{t,e,isen}$  is the exit total temperature if the inlet state undergoes an isentropic compression process to reach the same total pressure ratio. For the TUDa-GLR-OpenStage compressor, the relative error of the assumption is about 1.6% and 0.6% for 100% speed and 65% speed respectively, which are sufficiently small. For convenience, the approximately equal sign in Equation 1 will be replaced by the equal sign in the following deductions.

From the work of He and Zheng (2016), Equation 1 was extended to measure the accumulated loss of efficiency at an arbitrary location  $\mathbf{x}$ , as denoted in Equation 2:

$$\xi(\mathbf{x}) = \frac{T_{t,e}(S(\mathbf{x}) - S_i)}{c_p(T_{t,e} - T_{t,i})} \quad (2)$$

To compare the efficiency of two cases, an intuitive way is to calculate the efficiency deviation  $\Delta\eta(\mathbf{x}) = \xi(\mathbf{x})_{\text{case1}} - \xi(\mathbf{x})_{\text{case2}}$ . However, the flow domain of the two cases may not exactly overlap with each

other. To tackle this, the streamwise efficiency deviation in Equation 3 can be used instead:

$$\Delta\eta(m) = \xi(m)_{\text{case1}} - \xi(m)_{\text{case2}} \quad (3)$$

where  $\xi(m)$  is the mass-averaged loss of efficiency over a 2D plane perpendicular to the streamwise direction, and  $m$  represents the streamwise coordinate.  $\Delta\eta(m)$  is an effective indicator for the change of flow field: when  $d\Delta\eta/dm > 0$ , the local flow field at the streamwise coordinate  $m$  is improved in case 2 compared to case 1, and vice versa.

Likewise, the spanwise efficiency deviation is defined in Equation 4:

$$\Delta\eta(n) = \xi(n)_{\text{case1}} - \xi(n)_{\text{case2}} \quad (4)$$

where  $\xi(n)$  represents the circumferentially mass-averaged loss of efficiency over a 1D circular arc, which is located at the spanwise coordinate  $n$  and a specified streamwise location (usually the compressor exit). If  $\Delta\eta(n) > 0$ , then the local flow field at the spanwise coordinate  $n$  is improved in case 2 compared to case 1, and vice versa.

## Data availability statement

The data that support the findings of this study are available from the corresponding author upon reasonable request.

## Funding sources

Kailong Xia, Mingmin Zhu and Jinfang Teng acknowledge the support from the Natural Science Foundation of China (No. 51906140), the National Science and Technology Major Project (2017-II-0004-0017), the United Innovation Center (UIC) of Aerothermal Technologies for Turbomachinery and Innovation Fund from Engineering Research Center of Aerospace Science and Technology, Ministry of Education. Xiao He acknowledges the Imperial College President PhD Scholarship, the Henry Lester Trust and the Great Britain-China Educational Trust. The TUDA-GLR-OpenStage measurement campaign is supported by the EU-H2020 funded ARIAS project (No. 769346).

## Competing interests

Kailong Xia declares that he has no conflict of interest. Xiao He declares that he has no conflict of interest. Mingmin Zhu declares that he has no conflict of interest. Fabian Klausmann declares that he has no conflict of interest. Jinfang Teng declares that he has no conflict of interest. Mehdi Vahdati declares that he has no conflict of interest.

## References

- ANSYS (2021). Ansys CFX—Solver Theory Guide, Release 20.1: ANSYS Help DOC.
- Bakhtiari F., Wartzek F., Leichtfuß S., Schiffer H.-P., Goinis G., and Nicke E. (2015). Design and Optimization of a New Stator for the Transonic Compressor Rig at TU Darmstadt. In *Deutscher Luft- und Raumfahrtkongress 2015*.
- Beheshti B., Amaral Teixeira J., Ivey P., Ghorbanian K., and Farhanieh B. (2004). Parametric study of tip clearance—casing treatment on performance and stability of a transonic axial compressor. *Journal of Turbomachinery*. 126 (4): 527–535. <https://doi.org/10.1115/1.1791643>
- Bergner J., Kinzel M., Schiffer H.-P., and Hah C. (2006). Short length-scale rotating stall inception in a transonic axial compressor: experimental investigation. In *Turbo Expo: Power for Land, Sea, and Air*. ASME Paper No. GT2006-90209.
- Castillon L., Billonnet G., Riou J., Péron S., and Benoit C. (2014). A technological effect modeling on complex turbomachinery applications with an overset grid numerical method. *Journal of Turbomachinery*. 136 (10): 101005. <https://doi.org/10.1115/1.4027997>
- Chima R. V. (2009). SWIFT code assessment for two similar transonic compressors. AIAA Paper No. AIAA-2009-1058.
- Demargne A. A. J. and Longley J. P. (2000). The aerodynamic interaction of stator shroud leakage and mainstream flows in compressors. In *Turbo Expo: Power for Land, Sea, and Air*. ASME Paper No. 2000-GT-0570.
- Denton J. D. (1993). The 1993 IGTI scholar lecture: loss mechanisms in turbomachines. *Journal of Turbomachinery*. 115 (4): 10, pp. 621–656. <https://doi.org/10.1115/1.2929299>
- Denton J. (1997). Lessons from rotor 37. *Journal of Thermal Science*. 6 (1): 1–13. <https://doi.org/10.1007/s11630-997-0010-9>
- Denton J. D. (2010). Some limitations of turbomachinery CFD. In *Turbo Expo: Power for Land, Sea, and Air*. ASME Paper No. GT2010-22540.
- Gourdain N., Sicot F., Duchaine F., and Gicquel L. (2014). Large eddy simulation of flows in industrial compressors: a path from 2015 to 2035. *Philosophical Transactions of The Royal Society A: Mathematical Physical and Engineering Sciences*. 372 (2022): 20130323. <https://doi.org/10.1098/rsta.2013.0323>

- He X. and Zheng X. (2016). Mechanisms of lean on the performance of transonic centrifugal compressor impellers. *Journal of Propulsion and Power*. 32 (5): 1220–1229. <https://doi.org/10.2514/1.B36008>
- He X., Zhu M., Xia K., Fabian K. S., Teng J., and Vahdati M. (2023). Validation and verification of rans solvers for tuda-qlr-openstage transonic axial compressor. *Journal of the Global Power and Propulsion Society*. 7: 13–29. <https://doi.org/10.33737/jgpps/158034>
- Hoeger M., Fritsch G., and Bauer D. (1999). Numerical simulation of the shock-tip leakage vortex interaction in a HPC front stage. *Journal of Turbomachinery*. 121 (3): 456–468. <https://doi.org/10.1115/1.2841338>
- Klausmann F., Franke D., Foret J., and Schiffer H.-P. (2022). Transonic compressor Darmstadt - Open test case Introduction of the TUDa open test case. *Journal of the Global Power and Propulsion Society*. 6: 318–329. <https://doi.org/10.33737/jgpps/156120>
- Kröger G., Voß C., Nicke E., and Cornelius C. (2011). Theory and application of axisymmetric endwall contouring for compressors. In Turbo Expo: Power for Land, Sea, and Air. ASME Paper No. GT2011-45624.
- Lei V. M., Spakovszky Z. S., and Greitzer E. M. (2008). A criterion for axial compressor hub-corner stall. *Journal of Turbomachinery*. 130 (3): 031006. <https://doi.org/10.1115/1.2775492>
- Lu Y., Green J., Stapelfeldt S. C., and Vahdati M. (2019). Effect of geometric variability on running shape and performance of a transonic fan. *Journal of Turbomachinery*. 141 (10): 101012. <https://doi.org/10.1115/1.4044676>
- Menter F. R., Kuntz M., and Langtry R. (2003). Ten years of industrial experience with the sst turbulence model. *Heat and Mass Transfer*. 4: 456–468.
- Moore D. and Reid L. (1980). A performance of a single-stage axial-flow transonic compressor with rotor and stator aspect ratios of 1.19 and 1.26 respectively, and with design pressure ratio of 2.05. Tech. rep., NASA. NASA Report No. TP-1659.
- Muller M. W., Schiffer H.-P., Voges M., and Hah C. (2011). Investigation of passage flow features in a transonic compressor rotor with casing treatments. In Turbo Expo: Power for Land, Sea, and Air. ASME Paper No. GT2011-45364.
- Seshadri P., Parks G. T., and Shahpar S. (2014). Leakage uncertainties in compressors: the case of rotor 37. *Journal of Propulsion and Power*. 31 (1): 456–466. <https://doi.org/10.2514/1.B35039>
- Shabbir A., Celestina M. L., Adamczyk J. J., and Strazisar A. J. (1997). The effect of hub leakage flow on two high speed axial flow compressor rotors. In Turbo Expo: Power for Land, Sea, and Air. ASME Paper No. 97-GT-346.
- Sohn D. W., Kim T., and Song S. J. (2006). Influence of the leakage flow tangential velocity on the loss generation and leakage flow kinematics in shrouded axial compressor cascades. In Turbo Expo: Power for Land, Sea, and Air. ASME Paper No. GT2006-90979.
- Sun S., Chen S., Liu W., Gong Y., and Wang S. (2018). Effect of axisymmetric endwall contouring on the high-load low-reaction transonic compressor rotor with a substantial meridian contraction. *Aerospace Science and Technology*. 81: 78–87. <https://doi.org/10.1016/j.ast.2018.08.001>
- Thompson D., King P., and Rabe D. (1998). Experimental investigation of stepped tip gap effects on the performance of a transonic axial-flow compressor rotor. *Journal of Turbomachinery*. 120 (3): 477–486. <https://doi.org/10.1115/1.2841743>
- Wellborn S. R. and Okiishi T. H. (1999). The influence of shrouded stator cavity flows on multistage compressor performance. *Journal of Turbomachinery*. 121 (3): 486–497. <https://doi.org/10.1115/1.2841341>
- Wisler D. and Beacher B. (1989). Improved compressor performance using recessed clearance (trenches). *Journal of Propulsion and Power*. 5 (4): 469–475. <https://doi.org/10.2514/3.23178>
- Zhu M., Teng J., Qiang X., Feng J., and Feng J. (2019). Impact of hub gap leakage on stator endwall flow in an axial compressor stage with casing treatment. *Aerospace Science and Technology*. 94: 105399. <https://doi.org/10.1016/j.ast.2019.105399>